---

# Transition-metal dichalcogenide $NiTe_2$: an ambient-stable material for catalysis and nanoelectronics

Silvia Nappini[1,§], Danil W. Boukhvalov[2,3,§], Gianluca D'Olimpio[4], Libo Zhang[5], Barun Ghosh[6], Chia-Nung Kuo[7], Haoshan Zhu[8], Jia Cheng[9], Michele Nardone[4], Luca Ottaviano[4], Debashis Mondal[1], Raju Edla[1], Jun Fuji[1], Chin Shan Lue[7], Ivana Vobornik[1], Jory Yarmoff[8], Amit Agarwal[6], Lin Wang[5], Lixue Zhang[9], Federica Bondino[1], and Antonio Politano[4,10,*]

*1 Consiglio Nazionale delle Ricerche (CNR)- Istituto Officina dei Materiali (IOM), Laboratorio TASC in Area Science Park S.S. 14 km 163.5 34149 Trieste, Italy*
*[2] College of Science, Institute of Materials Physics and Chemistry, Nanjing Forestry University, Nanjing 210037, P. R. China*
*[3] Theoretical Physics and Applied Mathematics Department, Ural Federal University, Mira Street 19, 620002 Ekaterinburg, Russia*
*4 Department of Physical and Chemical Sciences, University of L'Aquila, via Vetoio, 67100 L'Aquila (AQ), Italy*
*5 State Key Laboratory of Infrared Physics, Shanghai Institute of Technical Physics, Chinese Academy of Sciences, 500 Yutian Road, Shanghai 200083, China*
*6 Department of Physics, Indian Institute of Technology Kanpur, Kanpur 208016, India*
*7 Department of Physics, National Cheng Kung University, 1 Ta-Hsueh Road, 70101 Tainan, Taiwan*
*8 Department of Physics and Astronomy, University of California, Riverside, Riverside, CA 92521, United States*
*9 College of Chemistry and Chemical Engineering, Qingdao University Qingdao 266071, Shandong, China*
*10 CNR-IMM Istituto per la Microelettronica e Microsistemi, VIII strada 5, I-95121 Catania, Italy*

*antonio.politano@univaq.it;

§ These authors contributed equally

## Abstract

*By means of theory and experiments, we assess the application capability of nickel ditelluride ($NiTe_2$) transition-metal dichalcogenide in catalysis and nanoelectronics. The Te surface termination forms a $TeO_2$ skin in an oxygen environment. In ambient atmosphere, passivation is achieved in less than 30 minutes with the $TeO_2$ skin having a thickness of about 7 Å. $NiTe_2$ shows outstanding tolerance to CO exposure and stability in water environment, with subsequent good performance in both hydrogen and oxygen evolution reactions. $NiTe_2$-based devices consistently demonstrate superb ambient stability over a timescale as long as one month. Specifically, $NiTe_2$ has been implemented in a device that exhibits both superior performance and environmental stability at frequencies above 40 GHz, with possible applications as a receiver beyond the cut-off frequency of a nano-transistor.*

Keywords: Nickel ditelluride; transition-metal dichalcogenides; surface science; density functional theory; catalysis

## Main text

Following the advent of graphene, the scientific community has widely investigated a large number of two-dimensional and layered materials, which have been shown to be effective for a myriad of applications in nanoelectronics [1, 2], energy storage [3, 4], sensing [5], gas separation [6] and seawater desalination [7]. An especially important class of materials are transition-metal dichalcogenides (TMDs) $MX_2$, which consist of a transition-metal atom (denoted as M) from groups 4–10 and a chalcogen (denoted as X, which can be S, Se, or Te). Each $MX_2$ layer is held together by strong covalent bonds, while interlayer bonds are due to weak van der Waals forces. Therefore, TMDs are cleavable down to an atomically thick single layer. TMDs can also host topologically protected electronic states. As an example, $MoTe_2$ is a type-II Weyl semimetal [8], while $PtTe_2$ [9, 10] and $PdTe_2$ [11, 12] are type-II Dirac semimetals. Their Ni-based counterpart, $NiTe_2$, has also been predicted to be a type-II Dirac semimetal [13]. Notably, the abundance on Earth of Ni compared to Pt and Pd makes $NiTe_2$ more economic and, correspondingly, more suitable than $PtTe_2$ and $PdTe_2$ for large-scale technological applications. Recently, $NiTe_2$ has been shown to exhibit the planar Hall effect [14] and to possess a remarkable value of the breakdown current density (up to $4.7 \times 10^7$ A/cm$^2$ ) [15]. Other recent studies have highlighted the capabilities of this material as an electrochemical sensor for glucose detection[16] and for urea conversion [17].

Here, by means of several experimental techniques and density functional theory (DFT), the chemical reactivity and environmental stability of $NiTe_2$ is assessed to determine its suitability for potential applications in catalysis and nanoelectronics. Specifically, it is shown that $NiTe_2$ is a good candidate for CO-tolerant electrodes. While the high energy barrier for water decomposition inhibits the use of $NiTe_2$ in water splitting and oxygen reduction reactions, the stability of $NiTe_2$ in the presence of water makes it suitable for both hydrogen and oxygen evolution reactions. In ambient atmosphere, the Te termination evolves to a passivation layer of $TeO_2$ with a thickness of ~7 Å, which saturates in a

few minutes. Correspondingly, $NiTe_2$-based devices show current-voltage characteristics with negligible changes over a timescale of one month.

$NiTe_2$ crystallizes in the $CdI_2$-type trigonal (1T) structure with a P-3m1 space group (No. 164). $NiTe_2$ is a layered material in which each Ni atom in the basal plane is surrounded by six Te atoms, forming $NiTe_6$ octahedra. In this configuration, three atoms are present in each unit cell, as shown in Figs. 1a-b.

Two different surface terminations are feasible in principle: (i) a Te termination (Fig. 1a) or a NiTe termination (Fig. 1b), both of which have a hexagonal surface lattice (see top views in Supporting Information, SI, Fig. S1). The formation energies of Te-terminated and NiTe-terminated surfaces are 0.29 eV/$NiTe_2$ and 2.99 eV/NiTe, respectively, thus suggesting a prevalence for the Te-terminated surface.

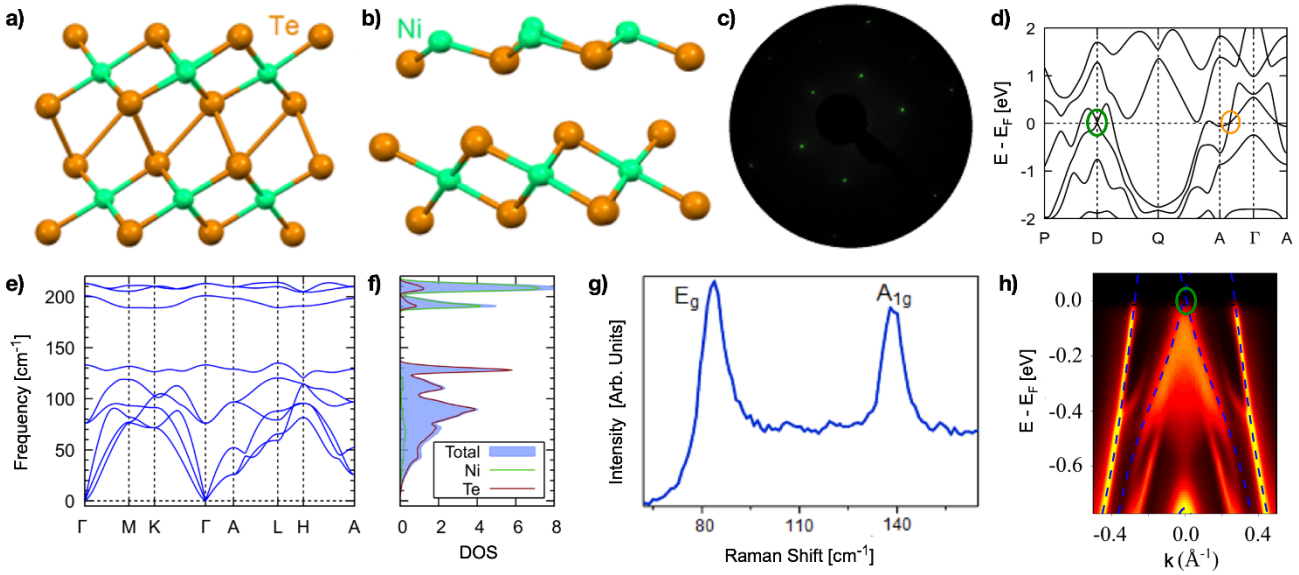


*Figure 1. Side views of (a) Te-terminated and (b) NiTe-terminated $NiTe_2$ surfaces. Panel (c) shows the LEED pattern, acquired at an electron energy of 84 eV. Panel (d) shows the electronic band structure of $NiTe_2$ clearly indicating the type-II Dirac node near the Fermi energy. The dispersion around each of the Dirac points is isotropic (green circle) in the horizontal P-D-Q plane (parallel to the experimental Γ-K-M plane) and anisotropic and "tilted" along the Γ − A direction (orange circle). Panels (e) and (f) show the phonon dispersion and phonon density of states for bulk $NiTe_2$, respectively. Panel (g) displays the Raman spectrum of $NiTe_2$ single crystal acquired at room temperature with laser wavelength λ=632.8 nm. Panel (h) shows the ARPES spectrum of $NiTe_2$ along the Γ-K direction, together*

*with the bulk bands calculated from first principles (dashed blue line). The Dirac point is indicated by a circle.*

Bulk $NiTe_2$ single crystals have a hexagonal surface symmetry, as evidenced by low-energy electron diffraction (LEED, Fig. 1c), and two Raman active bands at around 84 and 138 $cm^{-1}$ (Fig. 1g). These modes are assigned to $E_g$ and $A_{1g}$ phonons, respectively, on the basis of DFT calculations (see SI, Section S2, for more details) of phonon dispersion (Fig. 1e) and the corresponding density of states (Fig. 1f). Angle-resolved photoelectron spectroscopy (ARPES) is used to probe the electronic band structure of $NiTe_2$. In Fig. 1h, the measured band structure at the $k_z$ position nearest to the bulk Dirac point is shown along with the calculated bulk bands (dashed lines). Notably, the bulk Dirac point in $NiTe_2$ is in close proximity to the Fermi energy ($E_F$), contrary to $PdTe_2$ and $PtTe_2$ (see SI, Section S16 for a comparison). From ARPES experiments, we estimate that the Dirac point is located 20 meV above $E_F$, making $NiTe_2$ the most prominent TMD for the potential exploitation of Dirac fermiology.

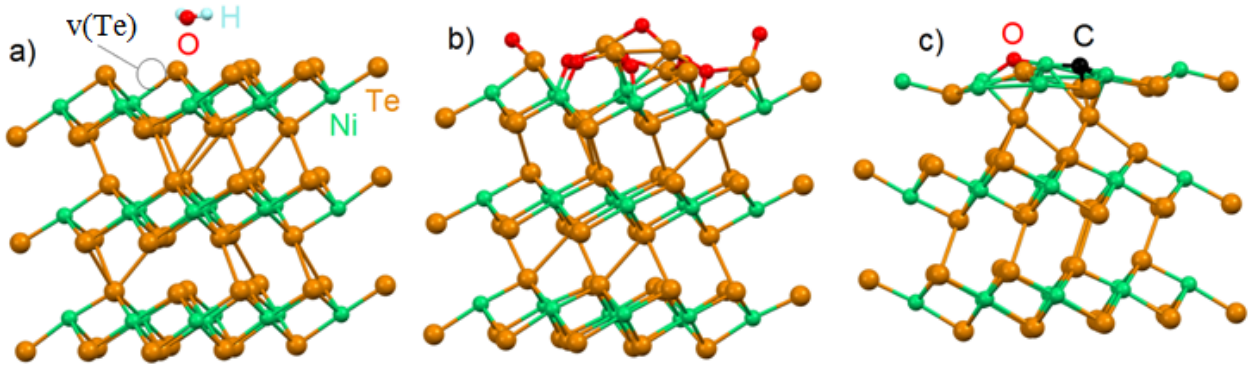


*Figure 2. Optimized atomic structure of physical adsorption of (a) water on $NiTe_2$ with one Te vacancy (denoted as "v(Te)"), (b) total oxidation of the Te-terminated undefected surface and (c) CO decomposition on NiTe-terminated surface.*

The energetics of adsorption and decomposition of various gases on different terminations of $NiTe_2$ surfaces are modeled to evaluate the stability and chemical reactivity of $NiTe_2$ (see Table I and Fig.

2). The $NiTe_{1.88}$ surface is also utilized to assess the role of surface defects, as it is basically a Te-terminated $NiTe_2$ surface with Te vacancies.

For the pristine Te-terminated surface at room temperature, only the physical adsorption of molecular oxygen is energetically favorable (differential Gibbs free energy ΔG of -43.3 kJ/mol), while water adsorption is metastable (ΔG=+3.1 kJ/mol) and carbon monoxide adsorption is energetically unfavorable (ΔG=+4.9 kJ/mol). Thus, $NiTe_2$ is particularly promising in the quest for novel electrode materials that overcome the problem of CO poisoning [18].

Te surface vacancies (Fig. 2a) favor the physical adsorption of molecular oxygen and stabilize the adsorption of carbon monoxide. The formation energy of a single Te vacancy on a Te-terminated surface (Fig. 1a) is 0.54 eV/Te. Therefore, the existence of Te vacancies is very likely in as-grown bulk single crystals, considering the fact that temperatures as high as 1050°C are employed during the growth (see Methods). Remarkably, it is found that water adsorption is also energetically unfavorable at room temperature on $NiTe_{1.88}$ , suggesting that surface vacancies do not act as adsorption sites. Conversely, a surface terminated with a NiTe monolayer would be extremely reactive toward most common gases, with stable adsorption of CO, $O_2$ and $H_2O$. Therefore, NiTe-terminated $NiTe_2$ electrodes would be poisoned by CO.

**Table I.** *Differential enthalpy ΔH and differential Gibbs free energy ΔG for the adsorption of CO, $H_2O$ and $O_2$ at room temperature on different types of $NiTe_2$ surfaces and their related decomposition energies.*

| Surface | Chemical species | ΔH for adsorption [kJ/mol] | ΔG for adsorption at room temperature [kJ/mol] | ΔH for decomposition [kJ/mol] |
|---|---|---|---|---|
| Te-terminated $NiTe_2$ | CO | -14.4 | +4.9 | - |
| | $O_2$ | -54.6 | -43.3 | -112.3 |
| | $H_2O$ | -28.8 | +3.1 | +169.9 |
| Te-terminated $NiTe_{1.88}$ | CO | -85.9 | -66.3 | - |
| | $O_2$ | -117.4 | -106.1 | +9.7 |

| | | | | |
|---|---|---|---|---|
| | $H_2O$ | -15.0 | +16.3 | +151.7 |
| NiTe-terminated $NiTe_2$ | CO | -134.4 | -115.1 | +94.7 |
| | $O_2$ | -40.9 | -29.6 | -58.8 |
| | $H_2O$ | -117.9 | -86.6 | +117.3 |

We also assess the possible decomposition (Figs. 2b,c) of adsorbed gases. Oxygen dissociation is energetically favorable for each possible $NiTe_2$ surface termination (except for Te-terminated $NiTe_{1.88}$), while the decomposition of water and carbon monoxide is energetically unfavorable in all cases. The oxidation of the whole surface layer (Fig. 2b) of Te-terminated $NiTe_2$ is particularly favorable ($\Delta H$ = -201.4 kJ/$O_2$). As the distance between the surface and sub-surface layers is rather small (2.77 Å), intercalation of molecular oxygen is rather improbable. Thus, complete oxidation of only the outermost $NiTe_2$ surface layer is feasible.

As $NiTe_2$ zigzag edges have an atomic structure similar to NiTe (see Fig. S1 in the SI), we can use the results for this kind of surface to estimate the chemical stability of the edges. Therefore, the decrease of the energy cost of water decomposition on NiTe-terminated surfaces suggests the possibility of water decomposition at the edges of Te-terminated $NiTe_2$.

To experimentally validate the theoretical results, experiments were carried out with a number of surface-sensitive techniques. Each of these probes a different property of the material, so that the combination of tools provides a good understanding of the surface physicochemical properties.

The surface termination of clean $NiTe_2$ at room temperature was determined using time-of-flight (TOF) low-energy ion scattering (LEIS, see SI, Section S3 for more details on the technique). Figure 3 shows TOF spectra collected along the $[10\bar{1}0]$ and $[2\bar{1}\bar{1}0]$ azimuthal orientations for as-cleaved $NiTe_2$. The main features in the spectra are the single scattering peaks (SSPs), which ride on a background of multiply scattered projectiles. The Ni and Te SSPs are at 4.3 and 3.7 μs, respectively. The Te SSP appears in both spectra, while the Ni SSP is absent in the spectrum collected along the $[10\bar{1}0]$ azimuth. The absence of a Ni SSP in the scattering along the $[10\bar{1}0]$ azimuth indicates that the as-cleaved $NiTe_2$ surface is terminated with Te, as this is a double alignment orientation that probes only the

outermost atomic layer due to shadowing and blocking of projectiles that scatter from deeper layers. If the surface had a NiTe termination, or was prepared in such a way as to produce such a termination, then a Ni SSP would be present. The observation of a Ni SSP in scattering along the single alignment $[2\bar{1}\bar{1}0]$ azimuth reveals that Ni is present in the second atomic layer.

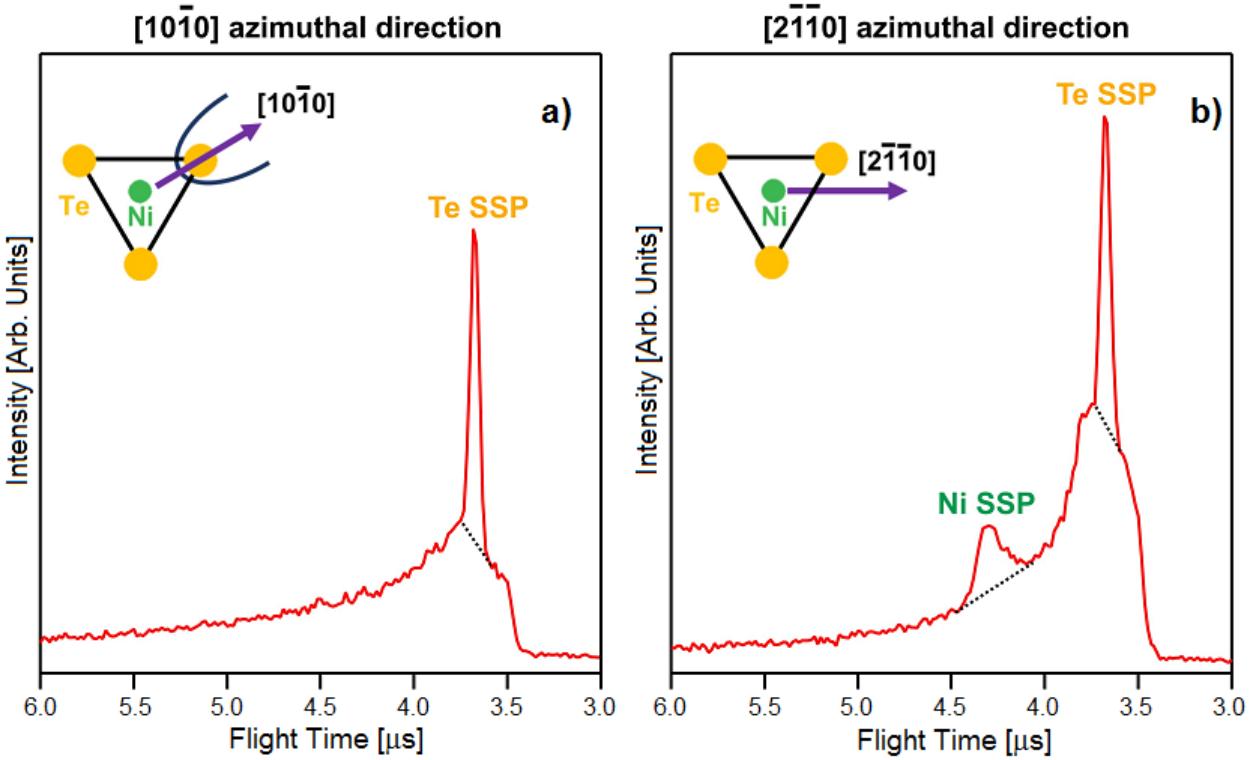


*Figure 3. LEIS time-of-flight (TOF) total yield spectra collected along the indicated azimuthal directions. The 3.0 keV $Na^+$ ion beam was incident at an angle of 40° from the surface plane and the detector is positioned at a scattering angle of 70°. The dashed lines illustrate the multiple-scattering background baselines. The insets show top-view schematics of the crystal unit cell along with projections of the azimuthal directions of the scattered beams.*

Surface chemical reactivity is assessed using high-resolution electron energy loss spectroscopy (HREELS) to measure vibrational modes. The as-cleaved $NiTe_2$ surface has a featureless vibrational spectrum, as seen in Fig. 4, thus excluding any intrinsic surface contamination. The absence of contamination was confirmed by an X-ray photoelectron spectroscopy (XPS) survey scan of the as-cleaved

sample (see SI, Fig. S4). Exposure to $2 \cdot 10^4$ L of CO and $H_2O$ at room temperature does not induce any vibrational peaks, thus indicating that the room-temperature sticking coefficient for these molecules is less than $10^{-3}$, in agreement with the expectations from theory in Table I. Conversely, the HREELS spectrum collected from $O_2$-dosed ($2 \cdot 10^4$ L) $NiTe_2$ at room temperature exhibits a vibrational band centered around 54 meV (434 $cm^{-1}$). This mode is ascribed to Te-O-Te bending vibrations, which are expected to occur at this energy [19]. This feature is still present in the vibrational spectrum after exposure to ambient atmosphere, together with a broad band centered at 91 meV, which involves a stretching vibration in $TeO_2$ [20]. After air exposure, CHx-derived modes from airborne contamination [21] are also observed. It should be noted that vibrational spectra of oxidized $NiTe_2$ strongly depend on the oxidation temperature. For example, when $O_2$ is dosed at higher temperature (T=700 K), the spectra also show a vibrational band arising from $TeO_3$ species [19]. Importantly, we note the absence of CO poisoning even after prolonged CO exposures, as demonstrated in experiments described in Section S15 of the SI.

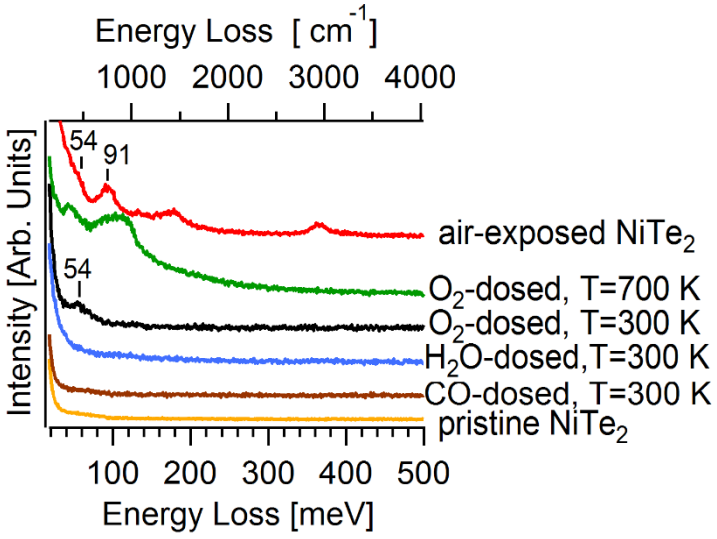


*Figure 4: HREELS spectra collected from the pristine, as-cleaved surface of $NiTe_2$ and after exposure to $2 \cdot 10^4$ L of CO, $H_2O$ and $O_2$ at T=300 K. For comparison, spectra collected after $O_2$ exposure at T=700 K and air exposure for one day are also shown. HREELS experiments were recorded in the*

*specular geometry with the incident angle fixed at 55° with respect to the sample normal. The primary electron beam energy was 3.5 eV. All of the HREELS spectra were recorded at T=300 K.*

High-resolution XPS spectra of the Ni-3p core levels for as-cleaved $NiTe_2$ and the same surface modified by the exposure to $2 \cdot 10^4$ L of CO, $H_2O$ and $O_2$ are reported in Fig. 5. Specifically, the binding energy (BE) of the of the Ni-3p spin-orbit split doublet (Fig. 5a) core level is recorded at 66.8 (J=3/2) and 68.5 (J=1/2) eV from the as-cleaved material. The doublet is practically unchanged upon CO exposure, while $H_2O$ adsorption attenuates the signal by 60%. Following $O_2$ exposure, the intensity of the Ni-3p level is reduced by 42% with the emergence of a new doublet with a J=3/2 component at 67.6 eV, which is associated with Ni(II) species [22], evidently related to Ni-O bonds. The intensity of this doublet is, however, just 11% of the total area of the Ni-3p signal. Likewise, analysis of Ni-2p spectra (SI, Fig. S6a) clearly indicates the formation of Ni-O bonds[23-25] on $O_2$-dosed $NiTe_2$.

Correspondingly, XPS of the Te-4d (Fig. 5b) core level for as-cleaved $NiTe_2$ shows two doublets with J=5/2 components at 39.8 and 40.2 eV, which arise from surface and bulk contributions, respectively. The observed BEs and energy splitting of these components are consistent with previous reports for Te-containing alloys [26, 27]. The Te-4d spectrum remains unchanged after CO exposure, while $H_2O$ dosage reduces the intensity (~35%) of the surface component and causes the appearance of a new doublet (J=5/2 at 40.7 eV), which can be ascribed to the formation of Te(0) species [28].

Strong changes of Te-4d spectrum occur after $O_2$ exposure, which induces oxidation of Te and the appearance of new components at higher BEs and a further reduction of the intensity of the surface component (which drops from 33% to 10% of the total spectral area). The appearance of novel doublets with $4d_{5/2}$ peaks at 43.6, 43.1 and 42.6 eV are ascribed to the formation of $TeO_2$ (10% of the total spectral area), TeO (15.5% of the total spectral area) and $TeO_x$ species (12.5% of the total spectral area) [28-30]. Similar conclusions are obtained from analysis of the Te-3d core level (SI, Fig. S6b).

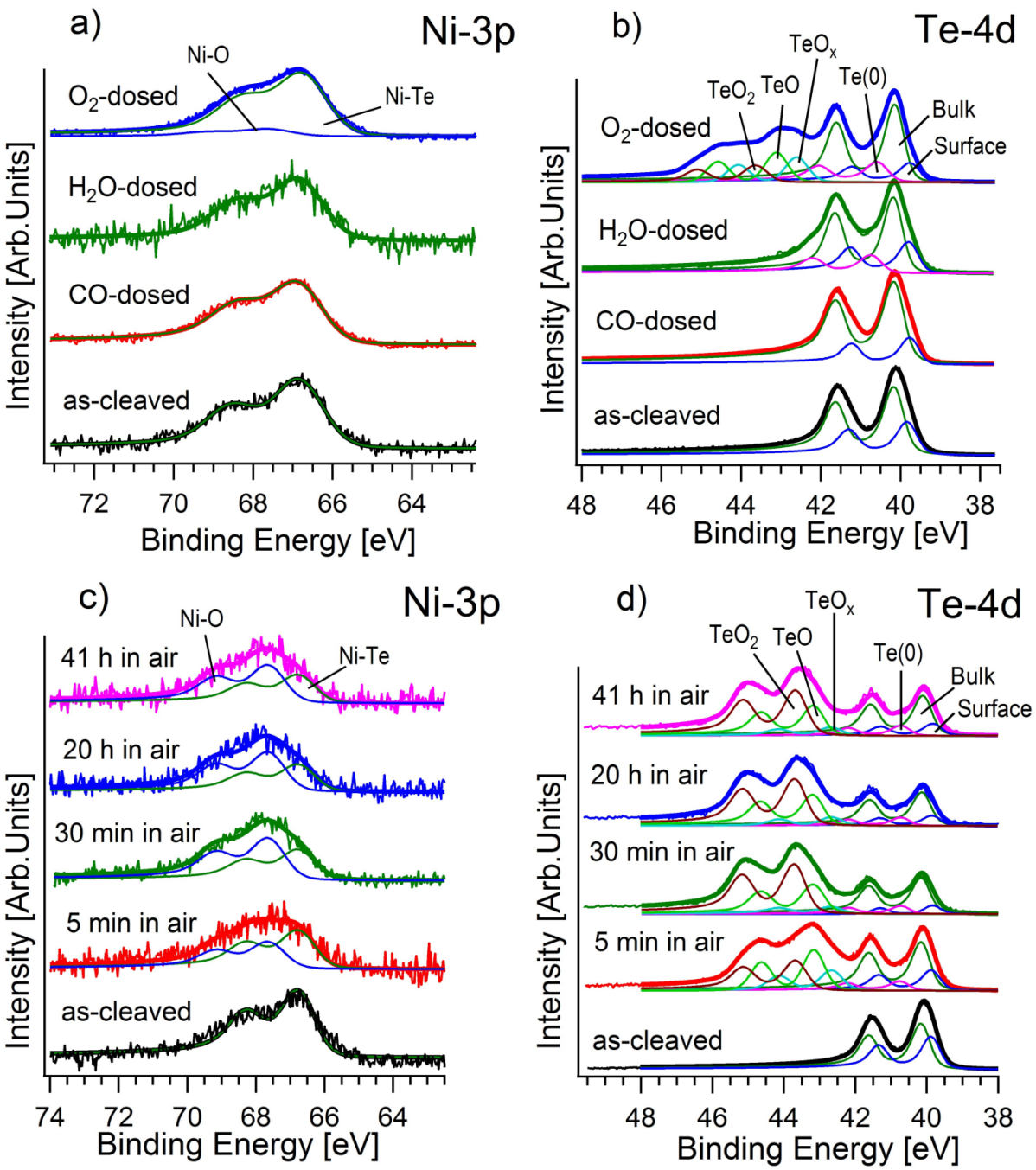


*Figure 5. (a) Ni-3p and (b) Te-4d XPS core level spectra collected from as-cleaved $NiTe_2$ (black curves) and from the same surface exposed to CO (red curves), $H_2O$ (green curves) and $O_2$ (blue curves). (c) Ni-3p and (d) Te-4d core level spectra collected from $NiTe_2$ exposed to air for 5 min (red curves), 30 min (green curves), 20 h (blue curves) and 41 h (magenta curves). The incident photon energy is 596 eV and the spectra are normalized to the maxima. The black curves collected from the as-cleaved sample are provided as a reference.*

The analysis of O-1s spectra (Fig. S7a in SI) indicates the absence of oxygen species in the CO-dosed sample, confirming the inertness of $NiTe_2$ toward CO as suggested by the Ni 3p and Te 4d spectra. Conversely, the O-1s core level of $H_2O$-dosed samples shows the presence of hydroxyl groups and molecular water [31-34]. The absence of water-related features in the HREELS spectrum in Fig. 4 suggests that $H_2O$ only adsorbs at steps, where water splitting occurs or, alternatively, it is intercalated into the subsurface region. Similar to the case of water-dosed epitaxial graphene[35], HREELS only detects water adsorbed above the surface due to its sensitivity only to the outermost surface layer[36]. For the $O_2$-dosed surface, the O-1s spectrum confirms the formation of an oxide species.

The effects of CO, $O_2$ and $H_2O$ gas exposure on the electronic properties of $NiTe_2$ were also assessed by measuring valence-band spectra (SI, Fig. S7b). The consistency of these spectra demonstrate that the electronic properties are negligibly affected by CO and $H_2O$ exposure, while $O_2$ dosage induces the valence band broadening due to O-2p states.

The as-cleaved $NiTe_2$ was also directly exposed to the atmosphere with the aim to assess its ambient stability. Ni-3p and Te-4d core-level spectra were collected as a function of exposure time to the atmosphere to study the aging of $NiTe_2$, as reported in Fig. 5c-d (see also SI, Fig. S8, for Ni-2p and Te-3d core-level spectra). A passivation layer of $TeO_2$ with a thickness ~7 Å is formed after only 5 minutes of air exposure. The surface oxide thickness was estimated from the oxide to metal peak ratio obtained from analysis of the Te 4d XPS data, applying a well-established procedure reported in the SI (Section S5). The intensity of the oxidization-related components gradually increases from ~40% (after 5 minutes in air) to ~60% (after 30 minutes in air) of the total spectral area. A prolonged exposure time (up to 41 hours) does not induce further oxidation of the $NiTe_2$ surface. Specifically, analysis of the Te-4d core level after 5 minutes in air indicates the formation of only a negligible amount of Te(0) species (5.7% of the total spectral area), together with $TeO_x$ species (11.5% of the

total area), TeO (29% of the total area), and $TeO_2$ (14% of the total area). The amount of Te(0) remains stable over time, while TeO (20%) and $TeO_x$ (6.5%) are both converted to $TeO_2$, which reaches 39% of the total Te-4d area after 30 minutes in air, without further changes after prolonged exposure times. Correspondingly, the Ni-3p core level displays a NiO-related component with an intensity of ~42% of the total spectral area after only 5 minutes in atmosphere. The NiO component reaches a maximum of 58% of the Ni-3p total spectral area after 30 minutes, and no further increase after a longer storage time in air is observed. Analysis of the O-1s core-level spectra (SI, Fig. S9a) indicates that the amount of surface oxide remains unchanged for exposure times longer than 30 minutes, while the intensities of components related to adsorbed $H_2O$ and C-OH contamination [37, 38] increase with time.

Air exposure also induces a shift of the Ni-derived states in valence-band spectra due to surface oxidation [39, 40] (see experimental data measured with a photon energy of 596 eV reported in Fig. S9b, and Fig. S11 for the assignment in the SI). Using a photon energy of 380 eV (SI, Fig. S10a), a broad feature at a BE of about 5 eV, which is associated with O-2p states [39], is also detected.

To track changes at a larger probing depth than XPS or HREELS, the Ni $L_{32}$ edge as a function of time in air was measured using X-ray absorption spectroscopy (XAS) by monitoring the total electron yield (TEY) (SI, Fig. S10b). The observation of minimal spectral changes in air-exposed samples due to surface oxidation [41] further supports the presence of a stable sub-nanometer passivation oxide layer.

To evaluate the environmental stability of $NiTe_2$, the evolution of atomic force microscopy (AFM) images of mechanically exfoliated flakes (Figs. 6a-d) was followed on a timescale of up to 10 days. The AFM results demonstrate that exposure to the atmosphere does not change the morphology of the flakes, as confirmed by the height profile along a specific direction remaining constant with exposure (Fig. 6e).

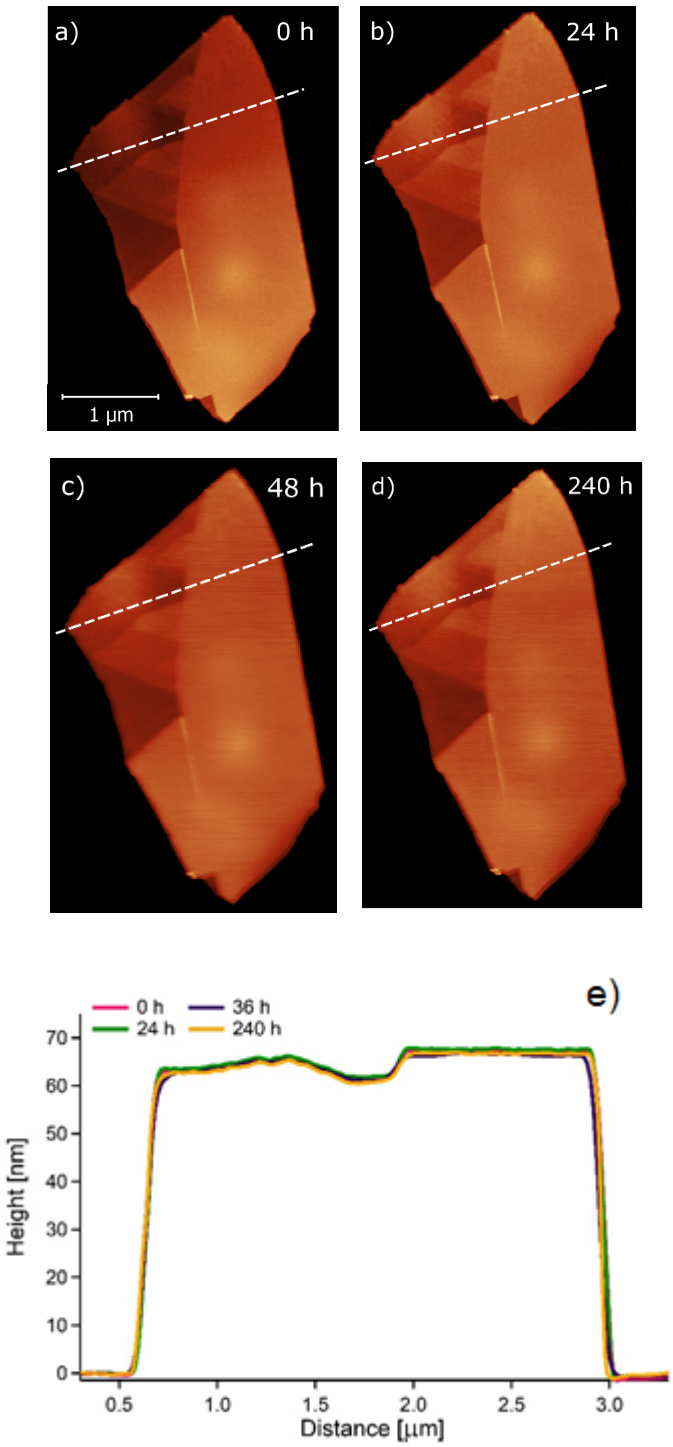


*Figure 6: Time evolution of AFM images of a ~60 nm thick flake of $NiTe_2$. Panel (a) shows the flake immediately after exfoliation, while panels (b)-(d) show the same flake after 24, 48 and 240 hours in air. The dotted white lines indicate the path of the height profile shown in panel (e).*

To validate the air stability of $NiTe_2$-based devices, photodetectors were fabricated using uncapped active channels of $NiTe_2$ (Figs. 7a-b). The output current and photocurrent versus voltage are reported in Figs. 7c-d, respectively. $NiTe_2$-based devices shows a negligible (albeit noticeable) decay in the output current over time. Specifically, the current drops from 2.42 to 2.35 mA at 100 mV (Fig. 7c) in 9 days, which is less than 3% of the original value. The small changes are ascribed to air-induced modifications to the metal-$NiTe_2$ interface rather than the active channel, on the basis of the AFM (Fig. 6) and XPS (Fig. 5c,d) aging experiments. For the sake of comparison, it is noted that in a similar device fabricated with black phosphorus (SI, Fig. S12), the output current decays by an order of magnitude in two weeks due to surface oxidation in air[42].

To further verify the air stability of $NiTe_2$ nanodevices, a high-frequency test was carried out to evaluate the generation-recombination noise associated with material degradation[43]. The suitability of $NiTe_2$ was tested for high-frequency electronics, specifically for the next generation of wireless communication networks that will operate at a higher data rate. We focus on the millimeter-wave band by demonstrating a novel mechanism of photodetection, based on hot electrons, to devise a receiver that works at a frequency higher than that of the transit-time mechanism operative in conventional transistors. To produce hot electrons, free carrier absorption due to intraband processes needs to be active, which depends on the band-gap and intrinsic carrier concentration of the specific material. The use of $NiTe_2$ is beneficial for intraband photon absorption, as shown in Fig. 7b [44]. A photocurrent will then arise following the unilateral diffusion of hot electrons under electrical bias. The $NiTe_2$-based device was subjected to electromagnetic radiation at a 40 GHz carrier-wave frequency, which has been proposed by Global Mobile Supplier Association [45] as the hotspot for the next interconnected communication system. The output of the fabricated device shows a good repetition ability with sharp rise and fall times, closely following the coded digital signal (Fig. 7e). The signal exhibits especially good repeatability without decay even after a one-month exposure to the ambient environment, thus elucidating the superb stability of a $NiTe_2$ device working at a frequency conservatively above the

cut-off frequency (12 GHz) of a transistor with a micrometer-long channel [46]. It is argued that the higher carrier frequency is associated with the high signal-to-noise ratio of our device (~$10^3$), which has possible relevance for devising next-generation high-band-width wireless communication [47] or in imaging applications [48].

The performance of millimeter-wave receivers based on $NiTe_2$ are compared with those of similar devices based on other gapless TMDs ($TaS_2$ and $TiTe_2$), graphene (semimetal) and black phosphorus (narrow-gap semiconductor) under the same conditions, with activated intraband absorption. Remarkably, $NiTe_2$-based device exhibits the best performance with responsivity above 2.5 A/W, as shown in Fig. 7f. It is worth noting that other TMDs semiconductors, such as $MoS_2$ and $WS_2$ with band-gaps greater than 1.2 eV [49], have intrinsic carrier concentrations that are insufficient to enable intraband photon absorption in the millimeter-wave region [46,47]. Explicitly, the cut-off frequency for $MoS_2$ is 6 GHz [50], which is much lower than the handling frequency of the hot-electron-based receiver in $NiTe_2$. A linear behavior of the photocurrent as a function of the incident power is found, as shown in Fig. 7g.

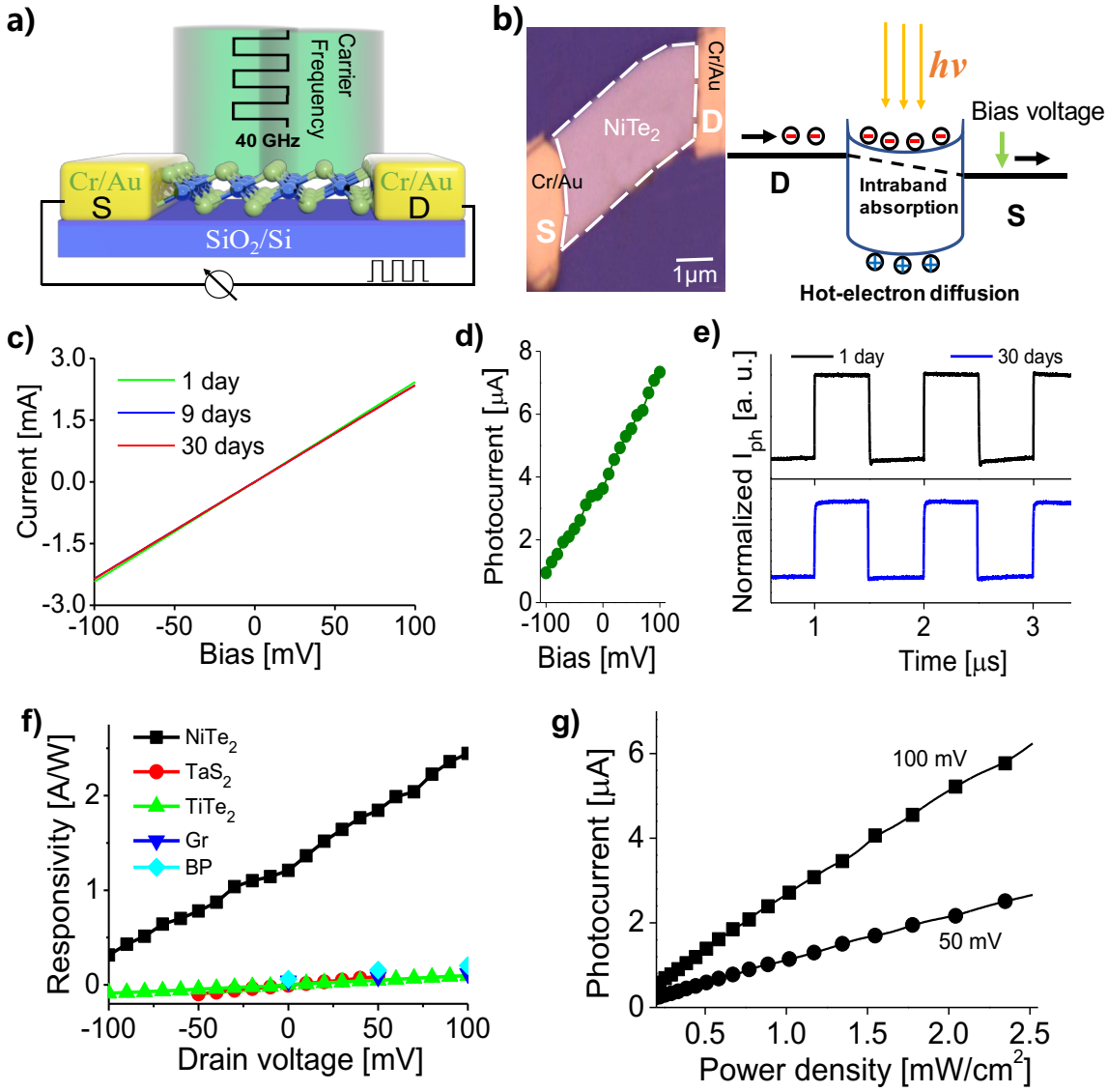


*Figure 7. a) Architecture of the $NiTe_2$ millimeter-wave receiver; b) Optical micrograph of the $NiTe_2$-based photodetector and band alignment of the device for hot-electron detection process; c) The I-V curve of the $NiTe_2$-based photodetector after one day (green curve), nine days (blue curve) and after 1 month in air (red curve); d) Photosignal of the $NiTe_2$-based photodetector under impingement of 40 GHz radiation; e) Time-resolved response of the as-prepared $NiTe_2$ millimeter-wave receiver (red curve) and after 1 month in air (blue curve). f) Bias dependence of sensitivity for $NiTe_2$-(black curve), $TaS_2$-(red curve), $TiTe_2$-(green curve), graphene-(Gr, light-blue curve) and black phosphorus-(BP, sky-blue curve) based devices; g) The incident power-dependence of photocurrent in the $NiTe_2$-based device at 40 GHz, showing linear behavior.*

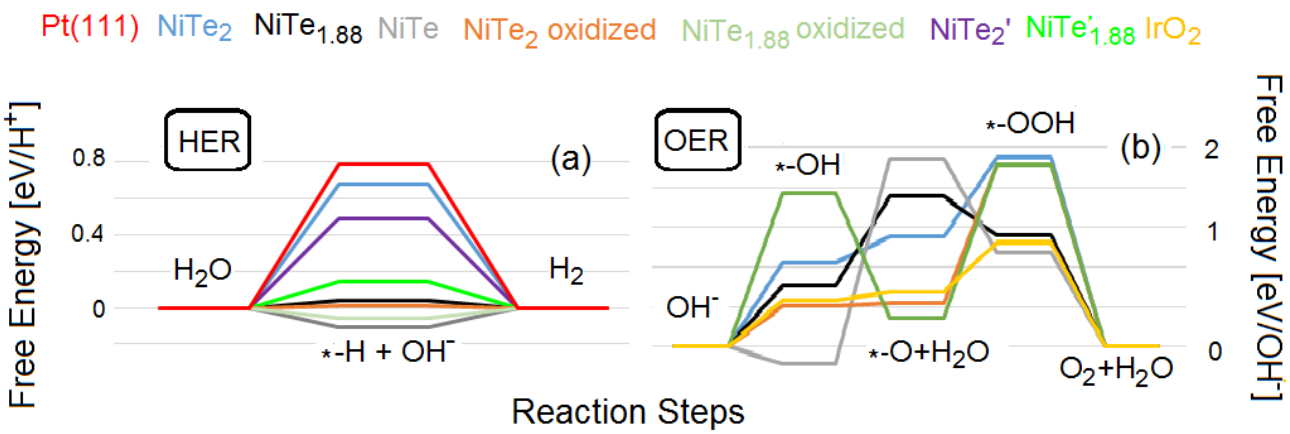


*Figure 8. Free energy diagrams for (a) HER and (b) OER in alkali media on various surfaces of $NiTe_2$. Results for whole hydrogen coverage when all active (Ni) sites on the surface participate in the reaction are marked by a prime symbol " ' ". Substrate is denoted by asterisk symbol "*".*

Finally, we model the performance of $NiTe_2$ in catalytic reactions by calculating the free energy for hydrogen and oxygen evolution reactions (HER and OER) on various $NiTe_2$ surfaces. Results were compared with Pt(111) and $IrO_2$(110) for HER and OER, respectively. For HER, the effects of hydrogen coverage and surface oxidation are considered. As the distance between hydrogen atoms adsorbed on Ni sites is rather large (3.85 Å), we exclude the Tafel reaction ($2*\text{-H} \rightarrow H_2$, where * corresponds to the substrate) from consideration. Thus, we assess the HER on $NiTe_2$ surfaces as a sequence of the reactions similar to Volmer and Herovsky reactions in acidic conditions:

1) $H_3O^+ + e^- \rightarrow *\text{-H} + H_2O$

2) $*\text{-H}_{ad} + H_3O^+ + e^- \rightarrow H_2 + H_2O$

Results of the calculations (Fig. 8a) demonstrate superiority of all kinds of $NiTe_2$ over Pt(111). In the case of $NiTe_{1.88}$ HER is almost barrier-free (0.04 eV). Oxidation of $NiTe_2$ makes HER in alkali media also very efficient and the magnitude of the free energy for this configuration is smaller than for Pt(111) in acidic media (~0.1 eV). For the OER in alkali media performance of pure $NiTe_2$ and $NiTe_{1.88}$ is worse than $IrO_2$(110). Each step requires more than 0.5 eV/$OH^-$ than over iridium oxide. Oxidation of $NiTe_2$ surface makes its catalytic performance on the first steps of OER in both media

similar to $IrO_2$(110) but the third step is energetically costly (Fig. 8b). Note that in the case of oxidized surface the last step of OER could be realized by other pathways. More details on the modelling of catalytic processes and on comparison with other TMDs are reported in Tables S2, S3 and Fig. S14 in the SI, Section S13.

The electrocatalytic activity of $NiTe_2$ single crystals towards the HER and OER was experimentally investigated by linear sweep voltammetry (LSV) in 1.0 M KOH (with iR-corrections). Although the overpotential at 10 mA $cm^{-2}$ is 520 mV, the onset potential for HER is only around -180 mV, indicating the good intrinsic HER activity of $NiTe_2$ bulk crystals. The Tafel slope of $NiTe_2$ single crystals towards HER was calculated to be 188.3 mV $dec^{-1}$ (the inset of Fig. 9a), and the sluggish kinetics is ascribable to $H_2$ bubbles that do not easily leave the surface of single crystal $NiTe_2$. The electrochemical durability, which is an important parameter in assessing the electrocatalytic performance in practical applications, was also tested. The chronoamperometric measurement for $NiTe_2$ single crystals at a constant potential of -0.47 V (vs RHE) ensures good durability of its current density for a time period extending up to 15 h (Fig. 9b). Concerning the OER activity, an overpotential of 410 mV is required to reach 10 mA $cm^{-2}$, while the Tafel slope is 106.9 mV $dec^{-1}$ (inset of Fig. 9c), thus indicating a good OER activity. The chronoamperometric curve of a $NiTe_2$ single crystal electrode at 1.64 V indicates durability for about 45 h (Fig. 9d).

Although HER and OER results for bulk single crystals indicate high activity and electrode durability, the exfoliation of the $NiTe_2$ single crystal in liquid phase to produce nanosheets or, alternatively, the synthesis of $NiTe_2$ nanoparticles is expected to significantly improve the HER and OER activities due to the higher number of active sites and, correspondingly, a higher surface-to-volume ratio.

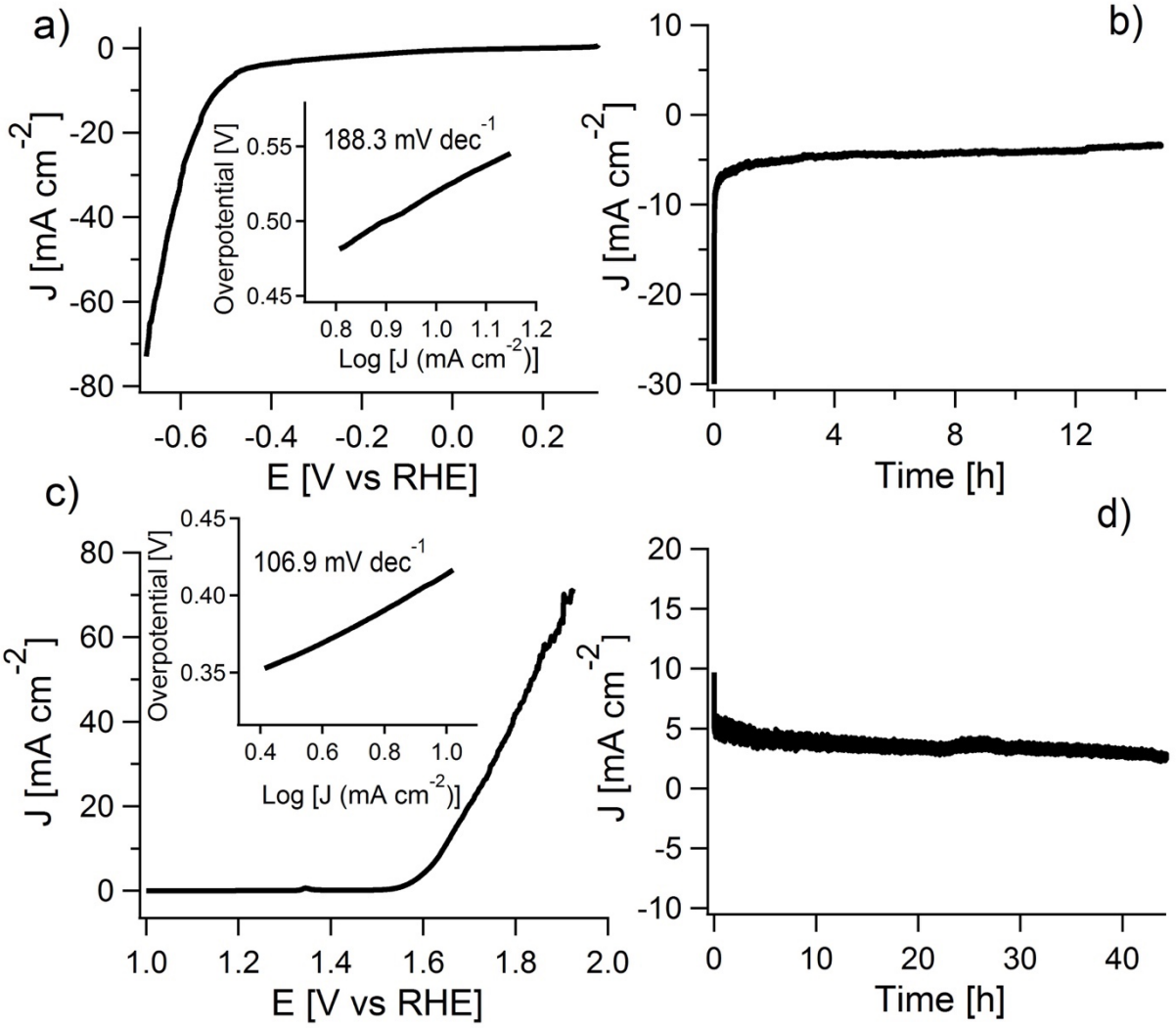


Figure 9. a) LSV curve and the corresponding Tafel plot of $NiTe_2$ single crystal towards HER in 1.0 M KOH, scan rate: 2 mV $s^{-1}$. b) The chronoamperometric curve of $NiTe_2$ single crystal in 1.0 M KOH at -0.47 V vs. RHE. c) LSV curve and the corresponding Tafel plot of $NiTe_2$ single crystal towards OER in 1.0 M KOH, scan rate: 2 mV $s^{-1}$. d) The chronoamperometric curve of $NiTe_2$ single crystal in 1.0 M KOH at 1.64 V vs. RHE.

**Conclusions**

It is demonstrated that bulk $NiTe_2$ is an ambient-stable material with diverse applications, ranging from catalysis to nanoelectronics. A passivating $TeO_2$ overlayer (thickness ~7 Å) is formed after exposure to ambient atmosphere for less than 30 minutes. The passivated surface is stable in air over a timescale of several weeks. The $NiTe_2$ surface does not show any reactivity toward $H_2O$ and CO, enabling the possibility to fabricate CO-tolerant electrodes for electrocatalysis that would be stable in

an aqueous environment. The catalytic applications of $NiTe_2$ for the HER and OER in water media are particularly feasible. Definitely, $NiTe_2$ single crystal showed promising electro-catalytic activity toward both HER and OER in alkaline environment, as well as high electrode durability. These results pave the way to the use of $NiTe_2$ as a low-cost electrocatalyst. The influence of Te vacancies and surface oxidation on the catalytic activity of $NiTe_2$ is also described.

Furthermore, devices with active $NiTe_2$ channels exhibit high stability in air without the need for encapsulation. Specifically, a $NiTe_2$-based high-frequency receiver was fabricated that exhibits both a fast response data rate of 40 GHz and high sensitivity (responsivity of ~2.5 A/W with signal-to-noise ratio of $\sim 10^3$), with negligible changes after air exposure for more than one month. In particular, the high-frequency receiver is able to detect carrier frequencies above 40 GHz, thus paving the way for the use of $NiTe_2$ for compact or even flexible integration for future communication or imaging systems.

## Methods

### Computational method and model

The atomic structure and energetics of various configurations of various gases adsorbed on $NiTe_2$ were studied by DFT using the QUANTUM-ESPRESSO code [51] and the GGA–PBE + van der Waals (vdW) approximation, which is feasible for the description of adsorption of molecules on surfaces [52, 53]. We used energy cutoffs of 25 and 400 Ry for the plane-wave expansion of the wave functions and the charge density, respectively, and the 4×4×3 Monkhorst-Pack *k*-point grid for the Brillouin zone sampling [54]. For modelling the $NiTe_2$ surface, we used a slab of three layers.

Physisorption enthalpies were calculated by the standard formula:

$$\Delta H_{phys} = [E_{host+mol} - (E_{host} + E_{mol})],$$

where $E_{host}$ is the total energy of the pristine surface, and $E_{mol}$ is the energy of a single molecule of the selected species in an empty box. In the case of water adsorption, only the gaseous phase is considered. The chemisorption energy is defined as the difference between the total energy of the system with an adsorbed molecule and the total energy of the same system after decomposition of the same molecule on the surface. For the case of physisorption, we also evaluated the differential Gibbs free energy by the formula:

$$\Delta G = \Delta H - T\Delta S,$$

where T is the temperature and $\Delta S$ is the change of entropy of the adsorbed molecule. The entropy was estimated considering the gas-to-liquid transition by the standard formula:

$$\Delta S = \Delta H_{vaporisation}/T,$$

where $\Delta H_{vaporization}$ is the measured enthalpy of vaporization. All formulas and technical details for the calculations of the HER and OER are the same as used for the modeling of these reactions over a Pt(111) substrate[55, 56]. A value for the overpotentials of U = 1.23 and 0.89 eV was used for OER in acidic and alkali medium, respectively.

**Single-crystal growth**

Single crystals of $NiTe_2$ were grown using the Te flux method. We used various molar ratios of Ni to Te, ranging from 1 : 3 to 1 : 30, finding an optimum ratio of 1 : 8. The mixtures of high-purity Ni powder (99.99%) and Te ingots (99.9999%) were sealed under vacuum in a quartz tube with a flat bottom. The quartz ampule was heated to 1050 °C over 10 hours, held at a constant temperature for 10 hours, and then slowly cooled to 600 °C at a rate of 3°C/h. It was finally annealed at this temperature for 100 hours to improve the quality of the crystals. The remaining Te flux was removed by centrifuging above 550°C. Several shiny plate-like single crystals with typical sizes of 8 × 8 × 1 $mm^3$ were harvested, which could be easily cleaved with adhesive tape. The flat surface of the crystal corresponds to the (001) plane. The crystal structure and phase purity of the as-grown crystals were identified by X-ray diffraction (XRD) (Bruker D2 PHASER) and Laue diffraction (Photonic Science) at room temperature. XRD analysis of powders and single crystals of $NiTe_2$ is extensively illustrated in SI, Fig. S12.

**Raman spectroscopy**

Micro-Raman spectra were acquired at room temperature by using a LABRAM spectrometer with a 1800 lines/mm diffraction grating equipped with a He–Ne laser source ( $\lambda$ = 632.8 nm) and an optical microscope with a 100x MPLAN with numerical aperture of 0.9. The laser spot cross diameter is ∼2 μm. The system operates in a back-scattering configuration.

**HREELS**

Vibrational experiments were carried out at room temperature with a Delta 0.5 spectrometer (Specs GmbH, Germany). The experimental resolution is 3-4 meV. Gases were dosed with precision leak valves.

### Synchrotron-radiation spectroscopies

XPS and XAS measurements were carried out on the CNR BACH beamline at Elettra Sincrotrone in Trieste (Italy). High-resolution XPS spectra were acquired using a VG-Scienta R3000 hemispherical analyzer at an emission angle of 60° from normal employing a photon energy of 596 eV for Ni-3p, Te-4d, O-1s and the valence band (also measured at 380 eV), and a photon energy of 1000 eV for the Ni-2p and Te-3d core levels. The overall energy resolution is 0.2 eV. Ni-3p, Te-4d, Ni-2p and Te3-d photoemission spectra were decomposed into spectral components using Doniach-Šunjić doublet line-shapes convoluted with a Gaussian profile, following a Shirley-type background subtraction. The O-1s core levels were decomposed using Voigt line-shape functions prior to a linear background subtraction.

XAS spectra at Ni L-edges were recorded in total electron yield mode (TEY) with an energy resolution of 0.2 eV. All spectra were measured at room temperature and the peak intensities were normalized to the incident photon flux.

## AFM

AFM images were acquired with a Digital D5000, Veeco system operating in Tapping-mode. The resonance frequency of the tip is 75 kHz.

### Device fabrication

Thin $NiTe_2$ flakes (with thickness around 70 nm) were obtained by mechanical exfoliation from bulk crystals and quickly transferred onto a 300 nm $SiO_2$/Si substrate. Electrodes were then patterned by ultraviolet lithography with a AZ5214 developer. Finally, 5-nm Cr/70-nm Au contacts were prepared

using electron-beam evaporation. The current-voltage characteristics of the fabricated devices were recorded at room temperature using an Agilent B2912A Semiconductor Analyzer.

**Electrochemical measurements.**

For HER and OER activity tests, experiments were performed on a Bio-Logic VSP-300 electrochemical workstation with a three-electrode configuration. $NiTe_2$ single-crystal plate was directly used as working electrode. Hg/HgO was used as the reference electrode. A graphite plate (for HER) or Pt wire (for OER) were used as counter electrode respectively. The linear sweep voltammetry (LSV) tests were carried out in 1M KOH at a scanning rate of 2 mV $s^{-1}$. The reported potentials were calibrated with reversible hydrogen electrode.

**Authors' contributions**

The project was conceived and coordinated by AP. XPS experiments were carried out by SN, FB and AP. AFM experiments were performed by GDO, under the supervision of LO. Raman experiments were performed by GDO and MN. HREELS experiments were carried out by AP. ARPES experiments were carried out by DM, JF and IV. Band-structure and phonon calculations were performed by BG and AA. Samples were grown by CSL, CNK, and AP. Chemical reactivity was modelled by DWB. LEIS experiments were carried out by HZ and JY. Electrocatalytic tests were performed by JC and LixZ. Microwave receiver was conceived and realized by LW and LibZ. The article was written by AP, with the contribution of the various authors for their part.

## References


[1] S.-S. Chee, W.-J. Lee, Y.-R. Jo, M. K. Cho, D. Chun, H. Baik, B.-J. Kim, M.-H. Yoon, K. Lee, M.-H. Ham, *Adv. Funct. Mater.* **2020**, 1908147.

[2] Z. Wang, P. Wang, F. Wang, J. Ye, T. He, F. Wu, M. Peng, P. Wu, Y. Chen, F. Zhong, R. Xie, Z. Cui, L. Shen, Q. Zhang, L. Gu, M. Luo, Y. Wang, H. Chen, P. Zhou, A. Pan, X. Zhou, L. Zhang, W. Hu, *Adv. Funct. Mater.* **2020**, *30*, 1907945.

[3] S. Shi, C. Sun, X. Yin, L. Shen, Q. Shi, K. Zhao, Y. Zhao, J. Zhang, *Adv. Funct. Mater.* **2020**, 1909283.

[4] Y. Cui, W. Liu, W. Feng, Y. Zhang, Y. Du, S. Liu, H. Wang, M. Chen, J. Zhou, *Adv. Funct. Mater.* **2020**, 1908755.

[5] R. Y. Tay, H. Li, J. Lin, H. Wang, J. S. K. Lim, S. Chen, W. L. Leong, S. H. Tsang, E. H. T. Teo, *Adv. Funct. Mater.* **2020**, 1909604.

[6] J. Shen, G. Liu, Y. Ji, Q. Liu, L. Cheng, K. Guan, M. Zhang, G. Liu, J. Xiong, J. Yang, W. Jin, *Adv. Funct. Mater.* **2018**, *28*.

[7] D. Pakulski, W. Czepa, S. D. Buffa, A. Ciesielski, P. Samorì, *Adv. Funct. Mater.* **2020**, *30*, 1902394.

[8] J. Jiang, Z. K. Liu, Y. Sun, H. F. Yang, C. R. Rajamathi, Y. P. Qi, L. X. Yang, C. Chen, H. Peng, C. C. Hwang, S. Z. Sun, S. K. Mo, I. Vobornik, J. Fujii, S. S. P. Parkin, C. Felser, B. H. Yan, Y. L. Chen, *Nat. Commun.* **2017**, *8*, 13973.

[9] M. Yan, H. Huang, K. Zhang, E. Wang, W. Yao, K. Deng, G. Wan, H. Zhang, M. Arita, H. Yang, *Nat. Commun.* **2017**, *8*, 257.

[10] A. Politano, G. Chiarello, B. Ghosh, K. Sadhukhan, C.-N. Kuo, C. S. Lue, V. Pellegrini, A. Agarwal, *Phys. Rev. Lett.* **2018**, *121*, 086804.

[11] H.-J. Noh, J. Jeong, E.-J. Cho, K. Kim, B. Min, B.-G. Park, *Phys. Rev. Lett.* **2017**, *119*, 016401.

[12] O. J. Clark, M. J. Neat, K. Okawa, L. Bawden, I. Marković, F. Mazzola, J. Feng, V. Sunko, J. M. Riley, W. Meevasana, J. Fujii, I. Vobornik, T. K. Kim, M. Hoesch, T. Sasagawa, P. Wahl, M. S. Bahramy, P. D. C. King, *Phys. Rev. Lett.* **2018**, *120*, 156401.

[13] C. Xu, B. Li, W. Jiao, W. Zhou, B. Qian, R. Sankar, N. D. Zhigadlo, Y. Qi, D. Qian, F.-C. Chou, X. Xu, *Chem. Mater.* **2018**, *30*, 4823.

[14] Q. Liu, B. Chen, B. Wei, S. Zhang, M. Zhang, F. Xie, M. Naveed, F. Fei, B. Wang, F. Song, *Phys. Rev. B* **2019**, *99*, 155119.

[15] B. Zhao, W. Dang, Y. Liu, B. Li, J. Li, J. Luo, Z. Zhang, R. Wu, H. Ma, G. Sun, Y. Huang, X. Duan, X. Duan, *J. Am. Chem. Soc.* **2018**, *140*, 14217.

[16] Y. Li, X. He, M. Guo, D. Lin, C. Xu, F. Xie, X. Sun, *Sens. Actuators B: Chem.* **2018**, *274*, 427.

[17] Z. Wang, P. Guo, M. Liu, C. Guo, H. Liu, S. Wei, J. Zhang, X. Lu, *ACS Appl. Energy Mater.* **2019**, *5*, 3363.

[18] Q. Li, R. He, J.-A. Gao, J. O. Jensen, N. J. Bjerrum, *J. Electrochem. Soc.* **2003**, *150*, A1599.

[19] S. Rada, M. Culea, E. Culea, *J. Non-Cryst. Solids* **2008**, *354*, 5491.

[20] A. Politano, G. Chiarello, C.-N. Kuo, C. S. Lue, R. Edla, P. Torelli, V. Pellegrini, D. W. Boukhvalov, *Adv. Funct. Mater.* **2018**, *28*, 1706504.

[21] Z. Li, Y. Wang, A. Kozbial, G. Shenoy, F. Zhou, R. McGinley, P. Ireland, B. Morganstein, A. Kunkel, S. P. Surwade, L. Li, H. Liu, *Nat. Mater.* **2013**, *12*, 925.

[22] K. Meeporn, N. Chanlek, P. Thongbai, *RSC Adv.* **2016**, *6*, 91377.

[23] M. Chhetri, S. Sultan, C. N. R. Rao, *Proc. Natl. Acad. Sci., U. S. A.* **2017**, 201710443.

[24] Q. H. Lu, R. Huang, L. S. Wang, Z. G. Wu, C. Li, Q. Luo, S. Y. Zuo, J. Li, D. L. Peng, G. L. Han, P. X. Yan, *J. Magn. Magn. Mater.* **2015**, *394*, 253.

[25] X. Li, M. Xin, S. Guo, T. Cai, D. Du, W. Xing, L. Zhao, W. Guo, Q. Xue, Z. Yan, *Electrochim. Acta* **2017**, *253*, 302.

[26] J. A. Leiro, M. H. Heinonen, S. Mattila, A. Szczerbakow, *Phys. Rev. B* **2006**, *73*, 205323.

[27] K. Ogawa, J. Azuma, K. Takahashi, M. Kamada, M. Sasaki, A. Ohnishi, M. Kitaura, H.-J. Kim, *Phys. Rev. B* **2012**, *85*, 165431.

[28] M. Bahl, R. Watson, K. Irgolic, *J. Chem. Phys.* **1977**, *66*, 5526.

[29] J. Sun, L. Fu, Y. Wang, J. Ren, Y. Li, W. Zhang, J. Zhu, *J. Appl. Phys.* **2013**, *114*, 083719.

[30] A. C. Galca, F. Sava, I. D. Simandan, C. Bucur, V. Dumitru, C. Porosnicu, C. Mihai, A. Velea, *J. Non-Cryst. Solids* **2018**, *499*, 1.
[31] P. R. Kidambi, B. C. Bayer, R. Blume, Z.-J. Wang, C. Baehtz, R. S. Weatherup, M.-G. Willinger, R. Schloegl, S. Hofmann, *Nano Lett.* **2013**, *13*, 4769.
[32] T. Schiros, L.-Å. Näslund, K. Andersson, J. Gyllenpalm, G. Karlberg, M. Odelius, H. Ogasawara, L. G. Pettersson, A. Nilsson, *J. Phys. Chem. C* **2007**, *111*, 15003.
[33] M. Fingerle, S. Tengeler, W. Calvet, T. Mayer, W. Jaegermann, *J. Electrochem. Soc.* **2018**, *165*, H3148.
[34] A. Grosvenor, B. Kobe, N. McIntyre, *Surf. Sci.* **2004**, *572*, 217.
[35] A. Politano, M. Cattelan, D. W. Boukhvalov, D. Campi, A. Cupolillo, S. Agnoli, N. G. Apostol, P. Lacovig, S. Lizzit, D. Farías, G. Chiarello, G. Granozzi, R. Larciprete, *ACS Nano* **2016**, *10*, 4543.
[36] H. Ibach, D. L. Mills, *Electron Energy Loss Spectroscopy and Surface Vibrations*, Academic Press, San Francisco 1982.
[37] A. Ganguly, S. Sharma, P. Papakonstantinou, J. Hamilton, *J. Phys. Chem. C* **2011**, *115*, 17009.
[38] S. Kerber, J. Bruckner, K. Wozniak, S. Seal, S. Hardcastle, T. Barr, *J. Vac. Sci. Technol. A* **1996**, *14*, 1314.
[39] A. Calloni, G. Berti, A. Brambilla, M. Riva, A. Picone, G. Bussetti, M. Finazzi, F. Ciccacci, L. Duò, *J. Phys.: Condens. Matter* **2014**, *26*, 445001.
[40] A. Visikovskiy, K. Mitsuhara, M. Hazama, M. Kohyama, Y. Kido, *J. Chem. Phys.* **2013**, *139*, 144705.
[41] H. Y. Peng, Y. F. Li, W. N. Lin, Y. Z. Wang, X. Y. Gao, T. Wu, *Sci. Rep.* **2012**, *2*, 442.
[42] A. Ziletti, A. Carvalho, P. E. Trevisanutto, D. K. Campbell, D. F. Coker, A. H. Castro Neto, *Phys. Rev. B* **2015**, *91*, 085407.
[43] Y. Fang, A. Armin, P. Meredith, J. Huang, *Nat. Photonics* **2019**, *13*, 1.
[44] P. Avouris, M. Freitag, *IEEE J. Sel. Top. Quantum Electron.* **2013**, *20*, 72.
[45] *Spectrum for Terrestrial 5G Networks: Licensing Developments*, Global Mobile Supplier Association, 2018.
[46] H. Wang, X. Wang, F. Xia, L. Wang, H. Jiang, Q. Xia, M. L. Chin, M. Dubey, S.-j. Han, *Nano Lett.* **2014**, *14*, 6424.
[47] E. C. Strinati, S. Barbarossa, J. L. Gonzalez-Jimenez, D. Kténas, N. Cassiau, C. Dehos, *arXiv:1901.03239* **2019**.
[48] S. Oka, H. Togo, N. Kukutsu, T. Nagatsuma, *Progress in Electromagnetics Research* **2008**, *1*, 197.
[49] G. Fiori, F. Bonaccorso, G. Iannaccone, T. Palacios, D. Neumaier, A. Seabaugh, S. K. Banerjee, L. Colombo, *Nat. Nanotechnol.* **2014**, *9*, 768.
[50] D. Krasnozhon, D. Lembke, C. Nyffeler, Y. Leblebici, A. Kis, *Nano Lett* **2014**, *14*, 5905.
[51] P. Giannozzi, S. Baroni, N. Bonini, M. Calandra, R. Car, C. Cavazzoni, D. Ceresoli, G. L. Chiarotti, M. Cococcioni, I. Dabo, A. Dal Corso, S. de Gironcoli, S. Fabris, G. Fratesi, R. Gebauer, U. Gerstmann, C. Gougoussis, A. Kokalj, L. Michele, L. Martin-Samos, N. Marzari, F. Mauri, R. Mazzarello, S. Paolini, A. Pasquarello, L. Paulatto, C. Sbraccia, S. Scandolo, G. Sclauzero, A. P. Seitsonen, A. Smogunov, P. Umari, R. M. Wentzcovitch, *J. Phys.: Condens. Matter* **2009**, *21*, 395502.
[52] J. P. Perdew, K. Burke, M. Ernzerhof, *Phys. Rev. Lett.* **1996**, *77*, 3865.
[53] V. Barone, M. Casarin, D. Forrer, M. Pavone, M. Sambi, A. Vittadini, *J. Comput. Chem.* **2009**, *30*, 934.
[54] H. J. Monkhorst, J. D. Pack, *Phys. Rev. B* **1976**, *13*, 5188.
[55] J. Greeley, T. F. Jaramillo, J. Bonde, I. Chorkendorff, J. K. Nørskov, *Nat. Mater.* **2006**, *5*, 909.
[56] Y. Tang, B. L. Allen, D. R. Kauffman, A. Star, *J. Am. Chem. Soc.* **2009**, *131*, 13200.